Physics of Plasmas ARTICLE pubs.aip.org/aip/pop

On-shot detection of fission isotopes of ^{238}U, produced by laser-driven x-rays

Cite as: Phys. Plasmas **32**, 073106 (2025); doi: 10.1063/5.0251735
Submitted: 4 December 2024 · Accepted: 27 June 2025 ·
Published Online: 14 July 2025

R. Kalla,[1,a)] P. Boller,[1,2,3] P. Tavana,[4,5] C. Brabetz,[2] J. Burggraf,[6,7] J. Cikhardt,[8] J. Glorius,[2] M. Gyrdymov,[2,5] Yu. A. Litvinov,[2,3] W. Nazarov,[9] J. Novotny,[8] U. Spillmann,[2] D. H. G. Schneider,[6] A. Yakushev,[2] A. Zylstra,[6] O. N. Rosmej,[2,3,5] T. Kuehl,[2,10] and V. Bagnoud[1,2,3]

AFFILIATIONS

[1]Technical University of Darmstadt, Darmstadt, Germany
[2]GSI Helmholtzzentrum für Schwerionenforschung GmbH, Darmstadt, Germany
[3]Helmholtz Forschungsakademie Hessen für FAIR, GSI Helmholtzzentrum für Schwerionenforschung, Darmstadt, Germany
[4]Friedrich Schiller University Jena, Jena, Germany
[5]Goethe University Frankfurt, Frankfurt am Main, Germany
[6]Lawrence Livermore National Laboratory, Livermore, California 94550-9698, USA
[7]Idaho State University, Pocatello, Idaho 83209, USA
[8]Czech Technical University in Prague, Prague, Czech Republic
[9]Independent Foam Target Supplier, St Andrews, United Kingdom
[10]Johannes Gutenberg University Mainz, Mainz, Germany

[a)]**Author to whom correspondence should be addressed:** rene.kalla.edu@gmx.de

ABSTRACT

This work presents the results of a nuclear fission experiment with depleted uranium, driven by ultra-intense multi-MeV bremsstrahlung, generated by laser-accelerated electrons in a high-Z converter, which enables the production of radioisotopes on the picosecond timescale. The advanced plasma target made of pre-ionized low-density foam enabled effective electron acceleration to energies of up to 100 MeV at a laser intensity of 10^{19} W cm^{-2} and the generation of ultra-bright bremsstrahlung with an effective temperature of 11.8 MeV in the giant dipole resonance region, with a previously unattained high conversion efficiency of 1%–2%. A major hazard in high-power laser experiments is the presence of harmful radiation and its impact on sensitive detectors. A gas flow system was used to transport volatile fission products from the laser-target interaction point to remote detectors in under ten seconds. This spatial separation of the detectors from the point of laser-matter interaction significantly reduces background noise, the impact of harmful radiation, and enables the detection of signals from short-lived radioisotopes—the products of induced nuclear fission—with high sensitivity.

I. INTRODUCTION

The ongoing development in laser-plasma physics allows for generating ultra-high fluxes of particles and secondary radiation reaching high-energy-density environments inaccessible before. The urge to step into the creation of such conditions is the investigation of particle states in high-energy, dense cosmic and astrophysical objects. These energy states can be fundamentally different from those on Earth. In many astrophysical environments, the energy density creates an overall averaged system of excited nuclei.[1] Investigating such excited nuclear states could provide new insights into reaction processes within these high-energy density environments.[1,2]

However, artificially creating reactions in these excited nuclear states is challenging due to the extremely short de-excitation timescales, which can reach down to femtosecond timescales.[3,4] This requires a rapid sequence of events. One possible approach is to combine the initial energy transfer for excitation and the reaction into a single particle species. This method necessitates high particle numbers in ultra-short bunch lengths. Using modern laser systems, high particle fluxes can be achieved.[5,6] The acceleration timescale in these systems is directly related to the laser pulse duration, which can be as short as a few femtoseconds.

Laser acceleration can employ various mechanisms depending on the target material properties and available laser pulse characteristics. The short laser pulse length in combination with the versatile tool box of acceleration mechanisms makes laser acceleration an excellent source for electrons, ultra-short MeV x-rays, positron pairs, neutrons, protons, and betatron radiation.[5–8] For electron acceleration, ultra-high fluxes and well-directed pulses of electrons can be achieved, which can then be converted into ultra-short X-ray beams after hitting a converter target.

A well-established acceleration mechanism for electrons is laser wake-field acceleration (LWFA). In LWFA, an intense laser field drives strong ponderomotive plasma waves, which can trap and accelerate electrons. This mechanism can accelerate electrons to energies up to a few GeV[9–11] with ever increasing bunch quality, such that applications in high-field physics or as driver for free electron lasers can now be envisioned. LWFA works optimally in underdense plasmas and with ultra-short laser pulses that are shorter than the plasma wavelength.[12–14]

Another mechanism, direct laser acceleration[5–8] (DLA), involves a relativistic laser forming a plasma channel with electron density just below the critical density. The resulting ponderomotive force causes the electrons to generate a self-induced quasi-static electromagnetic field, while the current of relativistic electrons generates a quasi-static azimuthal magnetic field. These fields lead to confinement of the relativistic electrons, which perform transverse betatron oscillations in the channel, by deflecting the outward-moving electrons in the direction of the laser beam axis.[14,15] These oscillations run along the polarization of the electric field of the laser pulse, so that efficient energy exchange is possible when the betatron frequency is close to the Doppler shifted laser frequency.

DLA can accelerate electrons to energies of 100 MeV. A major advantage of DLA over LWFA is the higher particle numbers in the accelerated bunch, which follows a Boltzmann-like distribution[12–14,16] and good conversion efficiency from the laser energy into particle kinetic energy. This method is highly efficient in near-critical-density plasmas with sub-picosecond laser pulses, such as those available at the Petawatt High Energy Laser for Ion eXperiments (PHELIX)[17] at GSI Helmholtzzentrum für Schwerionenforschung GmbH, Darmstadt, Germany, where a near critical density plasma was generated using low density polymer foams preheated by a separate ns-pulse.[5,6,18] This approach enabled an increase in the effective temperature and charge of the directed electrons by a factor of 10–15, compared to laser shots on conventional foil under the same laser parameters.[5,18] The DLA electrons penetrating high-Z converter materials, generated MeV bremsstrahlung with a half-opening angle of less than 20°, and up to 10^{11} photons (>10 MeV) measured in various DLA experiments.[5,6,19] The generation of high-energy bremsstrahlung radiation by laser accelerated electrons by the DLA process has developed substantially over the last few years. The outstanding benefit is the large number of electrons within a picosecond time window. In the present work, more than 10^{11} photons between 10 and 20 MeV were produced per pulse within a picosecond timeframe. The characteristic of bremsstrahlung, however, lacks the sensitive selection of the photon energy. In comparison, the high intensity gamma-ray source (HIGS) facility,[20–22] and the proposed facility at ELI-NP,[23] provide quasi mono-energetic and highly polarized photon beams within an energy range from 1 to 100 MeV. HIGS reaches up to 3×10^{10} photons/s. A major advantage of the DLA process is its ability to produce an in-pulse electron flux, which exceeds that of conventional electron acceleration by orders of magnitude.

In this paper, we propose and demonstrate that x-ray radiation, generated by DLA electron beams, can be used to study nuclear processes with existing high-power lasers at an intensity of 10^{19} W cm^{-2}. The large number of available photons allows for the investigation of low-reactivity interactions with these particles. Here, a photofission experiment on ^{238}U in the region of the giant-dipole resonance was performed, motivated by previous studies highlighting the potential of high-intensity photon sources for nuclear fission investigations.[24] The giant dipole resonance describes a collective excitation mode of the nucleus, occurring between 10 and 20 MeV for ^{238}U, which leads to increased photonuclear reaction probabilities.[25,26] For the detection of the produced fission fragments, we improved and employed a proven fission fragment transport system described in Ref. 8. It consists of a gas transport system, which swiftly transports the fission products to a detector located at a distance from the laser-plasma interaction environment. The detector is a germanium-based gamma spectrometer that records the gamma-radiation of the transported decaying fission fragments. In laser-driven experiments, damaging radiations like electromagnetic pulses (EMPs), fast neutrons, or prompt gammas/x-rays can occur and affect the durability and accuracy of the detectors. Here, the gas transport system enables reducing the background signal on the gamma detector significantly.

In the following, we first describe the experimental setup that allows for detecting laser-driven fission products. The emphasis is given to the secondary radiation conversion and characterization. The second part of the manuscript deals with the results on the characterization of the X-ray secondary source. This is followed by the analysis of the germanium detector spectra, where signals of the isotope ^{139}Xe are clearly visible, giving proof that bremsstrahlung-generated fission fragments can be quantitatively measured in a laser-plasma experiment.

II. EXPERIMENTAL SETUP

This section describes the experimental setup shown in Fig. 1. The experiment was conducted in single-shot mode at the

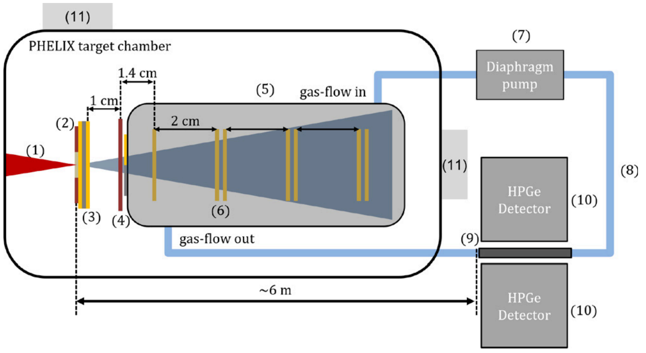

FIG. 1. Experimental setup with included dimensions between respective targets. (1) PHELIX, (2) foam target, (3) converter target (Au, Ta, Au) (4) activatable target (copper foil and gold and tantalum squares) (5) uranium container, (6) uranium targets, (7) diaphragm pump, (8) PTFE-tube system, (9) liquid-nitrogen cooled filter of activated carbon grains, (10) HPGe detector, (11) neutron bubble detector.

PHELIX[17,27] facility. The s-polarized PHELIX laser pulse with a duration of 750 ± 250 fs, central wavelength 1053 μm, and total energy of (75 ± 5) J was focused onto the pre-ionized target using a 150 cm focal length off-axis parabolic mirror. Within the full width at half maximum (FWHM) of the focal spot, an energy of (20 ± 2) J was measured, resulting in a peak intensity of approximately 10^{19} W cm^{-2}, and a normalized vector potential amplitude of $a_0 = 2.9$. To mitigate laser backreflection, the target normal was tilted by 10° relative to the incident laser axis. For this experiment, the PHELIX laser (1) is focused onto a CHO-foam target with a density of 15 mg cm^{-3}, held inside a copper washer. The benefit of PHELIX is its ability to create a well-controlled ns-pulse prior to the femtosecond main pulse, which can be tuned in energy and primary delay to the main pulse. This is crucial, as the foam target needs to be homogenized into a near-critical density (NCD) plasma. As foam targets can be fundamentally different in density, mass distribution, and in composition of the different elements, the tunable ns-pulse feature of PHELIX is excellent for finding the optimized settings for the used foams.

The PHELIX ns-pulse arrives 5 ns prior to the main pulse and has an energy that equals 3% of the main pulse energy. This corresponds to an average energy of 2.3 J in the ns-pulse settings. This ns-pulse forms an extended plasma with a density ramp from 0.01 n_{cr} to 3 n_{cr} over hundreds of mm inside the ultra-light foam (2), where $n_{cr} = 10^{21}$ cm^{-3} for the μm PHELIX wavelength.[28] Because of self-focusing of the laser in the low density pre-plasma, the laser intensity increases from 10^{19} W cm^{-2} in vacuum up to 2×10^{20} W cm^{-2} inside the relativistic plasma channel[29] allowing the direct laser acceleration in the plasma region also with an over-critical electron density. This ultra-short electron bunch is converted into intense x-rays inside a three-layered stack (3) of gold, tantalum, and gold plates with 1 mm thickness each, directly attached to the copper washer from the rear side. The thickness of the converter stack was optimized using Geant4[30] simulations, where the x-ray yield was evaluated for converter thicknesses of 0.1, 1, 3, and 5 mm, keeping the electron spectrum constant. A total thickness of 3 mm with high-Z materials provided the highest x-ray emission in the 7–70 MeV range,[5,19] which is relevant for giant dipole resonance studies. To ensure optimal experimental conditions, we varied the converter target thickness during prior measurements.

For the detection of the produced x-rays, an activatable target (4) is glued to the uranium container (5) flange, which contains the uranium targets (6). Figure 2 indicates the activatable target, which consists of a 100-mm-thick copper foil with attached squares of gold and tantalum with 1 mm thickness each. The activatable target, as well as the uranium container, are placed at the nearest possible position to the converter targets. Because of mounts and arrangements inside the PHELIX target chamber, the closest possible distance between the converter stack and the activatable targets could be achieved to be 10 mm. The activatable target serves as a monitor for MeV x-rays that pass through the uranium targets. When high-energy x-rays interact with ^{63}Cu, they can induce a (γ, n)-reaction, converting it to ^{62}Cu. By exposing the activated copper foil to a Bio-imaging Analyzer System Image Plate Multipurpose Standard (BAS-IP MS), the distribution of x-rays in the energy range of 14–21 MeV, corresponding to the FWHM of the ^{63}Cu (γ, n) ^{62}Cu reaction, can be visualized. Behind the copper foil, gold and tantalum targets are placed to measure the X-ray spectrum. As the MeV x-rays pass through these materials, they trigger (γ, xn)-reactions, each with different threshold energies. The amount of various isotopes of Au and Ta produced provides insights into the number of -rays at different energies. The cross-section-based method to use photon activation targets for flux and spectra analysis is a reliable fundamental method[31] and has been performed in previous experiments.[6,32,33] The integration of spatial distribution data from the copper foil with isotope yields from the Au and Ta samples enables a detailed characterization of the X-ray flux traversing the uranium targets.

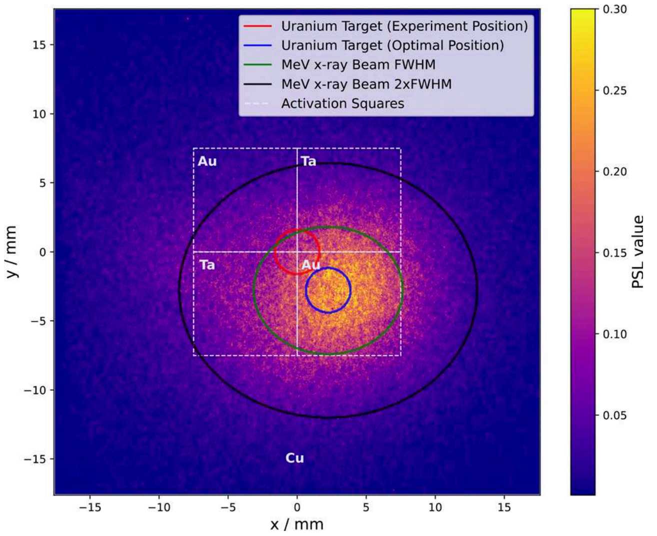

FIG. 2. Evaluated 14–21 MeV x-ray intensity distribution on the copper foil. The PSL-values describe the passing x-ray intensity seen by the copper foil in arbitrary units. A two-dimensional Gaussian function is fitted to the intensity distribution with the full width at half maximum (FWHM) (green) and the doubled FWHM (black). The actual position (red) as well as the optimal position (blue) of the first uranium target relative to the x-ray intensity distribution is marked. The squares of gold and tantalum targets with an edge length of 7.5 mm are indicated.

The fission fragments are produced inside the uranium targets, which are located inside the uranium container. The first uranium target is placed in the closest possible distance toward the container flange, which corresponds to a distance of 14 mm to the activatable target. The uranium targets consist of a stainless steel frame with a 15 mm-diameter hole. A micrometer-thin carbon foil is glued to the frame, and uranium-oxide (UO_2) is sputtered onto the carbon foil. This effectively results in uranium targets of 15 mm diameter with an average surface density of (1279 ± 6) μg cm^{-2} of depleted uranium.

X-rays passing through the uranium targets produce $(\gamma, \mathrm{fission})$-reactions inside the uranium portion of the UO_2-target. The stopping range for the produced fission fragments inside the uranium-oxide ranges from 5 to 10 μm, whereas the thickness of the sputtered uranium targets are on the order of μm. This ensures that the produced fission isotopes can escape the targets.

The space between the respective targets is filled with gas. For 2 bar gas mixtures of helium and argon, the stopping range for the emerging fission products is approximately 20 mm. All stopping ranges were calculated by a software package termed the *Stopping and Range of Ions in Matter*[34,35] (SRIM). Following these calculations, the next uranium target is placed 20 mm apart from the previous one, resulting in a total of seven uranium targets. The first target stands alone, while the remaining six are arranged in pairs, with the uranium-sputtered sides facing opposite directions. This configuration ensures that all uranium coatings are oriented toward the gas-filled space. The gas serves not only to stop the fission products but also acts as a transport medium for the fission fragments. In this experiment, we did not find any activation of the argon transport gas itself by the passing x-rays. Therefore, we used pure argon for most of the shots to simplify the refill process. The gas pressure of the mixture but also of pure argon was on the order of 2 bar.

A diaphragm pump (7) is driving a continuous gas flow inside the uranium container and flushes out the fission fragments. A PolyTetraFluoroEthylene (PTFE)-tube system (8) leads the fission fragments toward a liquid-nitrogen cooled filter of activated carbon grains (9). The filter temperature was maintained at $(-100 \pm 20)\,^\circ\mathrm{C}$ during the experiment. The fission fragments are stopped inside this filter. Two vis-à-vis oriented high-purity germanium (HPGe) detectors (10) detect the decay of the captured fission fragments. The distance between the detectors and the point of laser-matter interaction is around 6 m. The two HPGe detectors slightly differ in the size of the internal germanium crystal. With the dimensions of 52.7×58.2 and $63.8 \times 42\,\mathrm{mm}^2$ in diameter and length, the resulting unequal efficiencies between both detectors can be added to form a combined absolute efficiency coefficient to simplify the subsequent efficiency correction of the detected summed signals. This can be done because of the geometry between the detector heads and the filter of activated carbon grains which acts as the spatial radiation source. As the source is centered between the detector heads, the detection of a real event can only be detected by one detector. With this, the combined efficiency of both detectors for the experimental setup ranges from 17% to 1% for an energy range between 50 and 1500 keV. For signal processing, the data from the HPGe detectors is collected by a *versa module Europe* device. This device reads the detector signals in detector-separated channels and writes them in an event-separated way. For shielding purposes, a lead tower is built around the sensitive detector heads. Additionally, a metallic fleece shields the detectors and the electronic devices from damaging radiation. The construction of this setup is inspired by a similar setup successfully used in an earlier experiment.[8] In addition to this setup, two bubble detectors-personal neutron dosimeters (BD-PND) (11), sensitive to neutrons, are mounted onto the PHELIX target chamber: one in the axial direction and one in the radial direction regarding the point of laser-matter interaction and the laser axis. These devices detect the produced neutrons in the energy range from 200 keV to 15 MeV, which, in this experiment, mostly occur in (γ, xn)-reactions.

III. EXPERIMENTAL RESULTS

A. X-ray spectrum

The spectrum of the x-rays which irradiate the uranium targets is analyzed by combining activation data from a copper foil and squares of gold and tantalum with an edge length of 7.5 mm, as indicated in Fig. 2. X-rays passing through the copper foil leave an imprint of activated copper, which was analyzed to determine the spatial intensity distribution of the passing X-ray cone. An exemplary result for one shot is shown in Fig. 2. The intensity distribution was fitted with a two-dimensional Gaussian function. Using the position of the copper foil relative to the uranium targets and the origin of the x-rays, the projected size of the different uranium targets was calculated at the position of the copper foil.

This is illustrated in Fig. 2 for the first uranium target (red). Since the first uranium target also marks the central axis of this experiment, in respect to the laser axis, a slight shift in the X-ray cone orientation can be observed. This shift is represented by the percentage overlap of X-ray intensity seen by the first uranium target relative to the total X-ray intensity in the cone. The distance from the origin of the X-ray cone to the copper foil was 10 mm, and the distance from the copper foil to the first uranium target was 14 mm.

For the best shots, the average overlap of the first uranium target with the total X-ray cone was $(19.3 \times 42)\%$, indicating a well-directed X-ray cone. These shifts in the X-ray cone center are likely due to housing effects in the relativistic ion channel of the NCD-foam target. Figure 2 also reveals the opening angle of the X-ray cone by the fit of the two-dimensional Gaussian distribution. For the illustrated shot, the FWHM of the opening angle of the X-ray cone is 53.1°. The averaged FWHM of the opening angle of seven shots is $(47.7 \pm 43)^\circ$.

The detailed X-ray spectrum is used to calculate the expected fission yield of the individual uranium targets. Therefore, not only the intensity distribution but also the X-ray spectrum needs to be known. In this evaluation, we assumed the spatial distribution of the bremsstrahlung photons of different energies to be homogeneous within the X-ray cone. This can lead to underestimation of photon flux in the high-energy range of the X-ray spectrum. For measuring the energy spectrum of the x-rays, the 1 mm thick gold and tantalum squares behind the copper foil were used. The x-rays passing through these activation squares induced (γ, xn)-reactions, which have defined cross-section peaks at different energies (Fig. 3). This photon activation analysis is a powerful and convincing method used in the past.[19,36–39] By analyzing the detected neutron-deficient isotopes of gold and tantalum, we can estimate the number of x-rays across various energy ranges. In this experiment, we observed (γ, n) to $(\gamma, 5\mathrm{n})$ isotopes of gold and tantalum. The energy position of the deduced X-ray abundance producing each neutron-deficient isotope is estimated by the

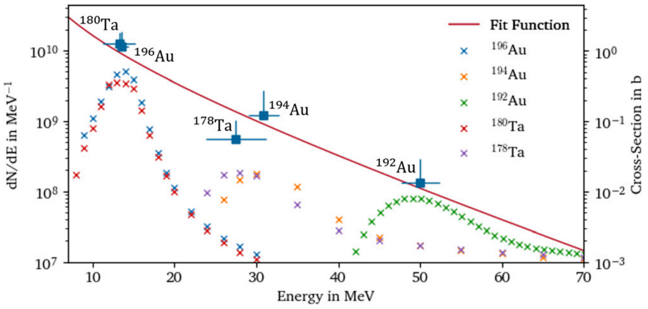

FIG. 3. Fitted x-ray energy spectrum with the applied fit function $\frac{A}{E} e^{-\frac{E}{T_e}}$. The blue square marked data point to the origin of the detected (γ, xn)-reactions in the gold and tantalum squares of the activatable target (Fig. 2). The x-errors show the FWHM of the cross-section peaks of the respective (γ, xn)-reactions forming the annotated isotopes. The asymmetric y-errors from the blue square markers largely arise from the fact that, at higher energies beyond the FWHM, there is still a possibility of nuclear reactions occurring. The fit function and the blue square markers refer to the left y-axis. The colored cross-markers for the labeled isotopes show the simulated cross-section peaks in b from the TALYS nuclear reaction model code.[40] These data points refer to the right y-axis.

peak position of the cross-section for this reaction type. The generation of bremsstrahlung with photon energies in the tens of MeV range is confirmed by the detection of ^{192}Au with a maximum cross-section around 50 MeV. The error in energy is defined by the FWHM of a Gaussian fit to each cross-section distribution.[19] The Gaussian fit accounts for over 75% of the total X-ray contribution within the region of interest. These fits do not describe the cross-section curves precisely as these cross-section distributions are not symmetric. As 75% of the influencing photons are included in the x-error, the y-error arises asymmetrically as a result of the underestimation of the influencing photons.

The resulting spectrum is shown in Fig. 3 and is fitted with an exponential function of $A/E \times e^{-\frac{E}{T_e}}$ with the corresponding amplitude $A = 3.86 \times 10^{11}$ and an effective temperature $T_e = 11.8$MeV. The fit was done in the range from 7 to 70 MeV. At low energies, the cross-section for photofission reactions in depleted uranium drops dramatically. At higher photon energies, the cross-section approaches a 10 mb level. However, the abundance of x-rays at higher energies also decreases significantly. Therefore, the focus is on the energy range from 7 MeV to slightly above 50 MeV. The most interesting region is around 14 MeV, where photofission has a cross-section peak for depleted uranium, which is shown in Fig. 4. The overlap of the energy-dependant X-ray abundance from Fig. 3 and the cross-section of the photofission process in depleted uranium from Fig. 4 shows high photon numbers in the region of the cross-section peak. Integrating the evaluated X-ray spectrum provides the total X-ray abundance per shot.

In this experiment, we produced an average of $(1.26 \pm 5) \times 10^{11}$ photons per shot. These large numbers are indicative of the potential to create a detectable number of fission fragments, even for experiments with low cross-section values in the mb regime like the one shown in Fig. 4. These numbers are in good agreement with the detected photon abundances from former experiments.[5,6,14] To calculate the expected total fission yield, we combined the overlap of the X-ray cone with the uranium targets and the X-ray spectrum itself. For a single shot X-ray spectrum, the total expected fission yield is given by the equation

$$Y = \frac{N_T}{A} \int_E \left(\sigma(E) \times \frac{dN}{dE} \right) dE. \qquad (1)$$

Here, the total expected fission yield Y is calculated using the target particle number N_T, the target surface area A (cm^2), and the energy integral of the cross-section $\sigma(E)$ (b) multiplied by the differential number of x-rays passing the uranium targets with respect to energy $\frac{dN}{dE}$ (MeV^{-1}). This resulted in a total expected fission yield of (12500 ± 4500) for the referenced shot of Figs. 2 and 3.

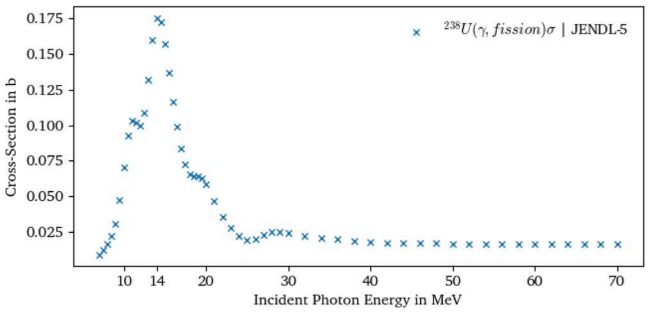

FIG. 4. Photofission cross-section of depleted uranium. The data points are taken from the Japanese Evaluated Nuclear Data Library version 5 (JENDL-5).[41] The data were evaluated with the CCONE code.[42]

B. Transported, collected, and detected ^{139}Xe

To compare the expected total fission yield with the actual detected yield of specific fission fragments, ^{139}Xe is a suitable candidate due to its prominent production in previous experiments[8] and its volatility, allowing it to be transported by the noble gas carrier medium. For transportation, the gas flow was started 5 min before the laser shot. The gas flow was stopped 30 s after the laser shot, assuming that all fission fragments were flushed toward the filter of liquid-nitrogen cooled activated carbon grains. The detection of the collected fission products in the filter began with the trigger of the laser shot. For the evaluation of ^{139}Xe, a total time of 160 s after the laser shot was analyzed, approximately four times the half-life of ^{139}Xe, allowing most of the xenon isotopes to decay, while limiting the background level.

The first concern in evaluating the fission fragment decay spectrum was the possible presence of disturbing radiation from the laser-matter interaction. As this radiation occurs almost instantaneously with the laser shot, and the perturbations like EMPs, high-energy photons, and fast neutrons travel near the speed of light, interference with the detectors is expected early during the first second after the laser shot. Despite placing the detectors about 6 m away from the laser-matter interaction point and shielding the detector heads with lead and EMP-fleece, interfering radiation was detected in the first second post-shot, seen as instantaneous peaks. At this time, no fission fragments could be transported from the uranium targets to the nitrogen-cooled filter due to the limited gas flow. By identifying the location of these interfering radiation peaks, we could isolate the fission fragment decay spectrum itself.

Figure 5 shows the fission fragment decay spectrum, highlighting different Xe isotopes. The unmarked peaks represent instantaneous peaks from the interfering radiation of the laser-matter interaction. The spectrum is averaged over the best shots of the experiment.

In the spectrum, the most prominent gamma line belongs to ^{139}Xe, with a main transition line at 219 keV. This transition line indicates the total produced xenon isotope not only from the fission process but also from its isobaric parents. This is because the parent

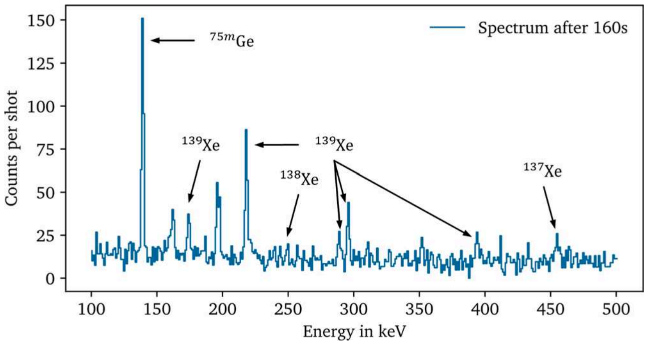

FIG. 5. Fission fragment decay spectrum of the combined detector signals accumulated over 160 s after the laser shot. The annotated Xe isotopes origin from the fission process except for ^{75m} Ge. This spectrum is averaged over seven shots.

isobars of ^{139}Xe, which decay into xenon, have very short half-lives. The longest half-lives of these parent nuclides are ^{139}I at 2.29 s and ^{139}Te at 0.72 s, with other half-lives in the millisecond range. In contrast to ^{139}Xe, these mentioned parent nuclides are nonvolatile isotopes. Therefore, the parent nuclides cannot be transported by the gas flow till their decay into ^{139}Xe. Since the uranium target chamber was flushed for 30 s immediately after the laser shot, and the shot-dependent calculated transportation time was between 3 and 8 s, nearly all parent nuclides decayed into ^{139}Xe during this time, allowing the resulting volatile xenon isotope to be transported to the filter as well. Therefore, the measured main transition line of xenon reveals the cumulative production of this xenon isotope. The term cumulative yield describes the total number of a specific isotope produced in a fission experiment, including those from the direct fission process and those from the decay of its isobaric parents. With a correction factor accounting for the transportation time T_t, measurement time T_m, and the transition probability p of the 219 keV line, the main transition line indicates a cumulative ^{139}Xe yield of (506 ± 100) atoms. A qualitative description of this correction factor $F(T_t, T_m, p)$ is given by the following equation:

$$F(T_t, T_m, p) = \frac{1}{p} \times \frac{e^{\lambda T_t}}{1 - e^{-\lambda(T_m - T_t)}}. \quad (2)$$

For the average cumulative yield of the best shots, this quantity modifies to (345 ± 31) ^{139}Xe atoms per shot.

In addition to the identified fission products with the xenon isotopes, the spectrum also shows ^{75m}Ge, a nucleus that does not arise directly from the fission process. This isotope is produced by the interaction of neutrons with the HPGe crystals of the detector heads. These neutrons originate from the interaction of our high-intensity X-ray beam with surrounding matter in the PHELIX laboratory, similar to the interaction of the x-rays with the gold and tantalum squares of the activatable target. The resulting (γ, xn)-reactions produce isotropically distributed neutrons, which then interact with the germanium crystal of the detector heads in (n, γ)-reactions. The decay of the produced germanium isotope can be seen in the fission fragment decay spectrum in Fig. 5.

With the identification of the fission fragments in the spectrum and the evaluation of the cumulative fission yield of ^{139}Xe, the cumulative fission yield and the total expected fission yield from the X-ray spectrum can be put in relation to each other. In our experiment, we additionally increased the gas flow rates to higher values for faster transportation times. Although the filter was cooled with liquid nitrogen, flushing the fission fragments out of the filter at higher gas flow rates might be possible. To evaluate possible flushing effects and the correlation between X-ray spectra and fission fragment decay spectra, we used the gas flow rates as weighting factors for the likelihood of flushing fission fragments. As transportation time is proportional to gas flow rates, lower gas flow rates result in fewer flushing forces within the filter, meaning longer transportation times directly indicate fewer flushing forces. Thus, transportation time can be considered as a weighting factor for the capturing probability of the total expected fission yield.

The new value of the product of transportation time and expected total fission yield can now be correlated with the actual detected ^{139}Xe isotopes. With this calculation, a correlation factor of 0.81 was calculated using Pearson's correlation coefficient. This suggests that different transportation times contribute to the correlation between total expected fission yield and actual detected ^{139}Xe isotopes, indicating possible flushing effects within the filter. Additionally, to this correlation value, the cumulative yield probability of ^{139}Xe, representing the ratio of detected ^{139}Xe nuclides to the total expected fission yield, is calculated. This value does not include any flushing effects of the filter. However, the average cumulative yield probability should minimize potential flushing effects in the averaging process. Therefore, the average cumulative yield probability of ^{139}Xe isotopes over the best shots is (2.62 ± 120)%.

Comparing this value with literature data is challenging because ^{139}Xe needs to be precisely detected, and the X-ray spectrum and/or total fission yield needs to be evaluated. For a detailed comparison, the X-ray spectra from both experiments should be similar, as the cumulative fission yield probability seems highly dependent on this spectrum. Despite these requirements, a more superficial comparison with an experiment by Foley and Yang was performed.[43] In their experiment, a LINAC-accelerated electron beam was converted into x-rays, which then caused fission in depleted uranium targets. A mechanical rail transported the uranium target to the detectors, where they measured the created fission fragments for different initial X-ray spectra. The X-ray spectra are classified by their cutoff energies, leading to cumulative yield probabilities for ^{139}Xe atoms for X-ray spectra with cutoff energies of 8, 14, and 20 MeV. The resulting values are shown in Table I.

In our experiment, the cutoff energy is beyond 70 MeV, so a direct comparison is not possible. Nevertheless, the data from Foley and Yang show a decreasing trend in cumulative yield probabilities for ^{139}Xe with increasing cutoff energies. Our calculated value follows this decreasing trend qualitatively.

C. Evaluation of additional fission-inducing reactions

In addition to the generation of high-energy x-rays, the experimental conditions also lead to the production of secondary particles, primarily neutrons and protons. These particles can, in principle, induce fission reactions in uranium nuclei and must therefore be considered as potential contributors to the observed isotope distribution. In the following, we first briefly assess the possibility of proton-induced fission. Then we provide a more detailed analysis of neutron-induced fission contributions.

TABLE I. Cumulative yield probability of ^{139}Xe isotopes for referenced x-ray cutoff energies.[a]

X-ray cutoff energy (MeV)	Cumulative yield probability (%)
8	(6.96 ± 44)
14	(4.67 ± 42)
20	(3.99 ± 24)
>70	(2.62 ± 120)

[a] This table shows the cumulative yield probabilities in % for ^{139}Xe isotopes for different x-ray spectra with referenced cutoff energies. The values for the x-ray cutoff energies of 8, 14, and 20 MeV are taken from Foley and Yang.[43] The last value in this table with the referenced cutoff energy of > 70 keV is deduced from our experiment.

In this experiment, proton production mainly occurs during the DLA process inside the NCD foam target. However, the contribution from proton-induced fission can be excluded based on geometric and material constraints. The range of sub-10 MeV protons in high-Z materials such as gold and tantalum is less than 1 mm, while the converter stack in our setup consists of 3 mm total thickness of Au and Ta layers, followed by an additional 5 mm stainless steel wall around the uranium container. In earlier experiments,[8] proton-induced fission was only observed if a 25 μm thin titanium entrance window was intentionally implemented into the uranium container.

Neutron production, on the other hand, cannot be spatially restricted, as high-energy photons generated in the setup interact with various components in the chamber, leading to neutron generation through secondary processes. Unlike protons, neutrons are able to penetrate much further and reach the uranium targets, potentially contributing to the measured fission yield decay signals. In the following, we therefore assess the possible impact of neutron-induced fission reactions on the isotope distribution observed in the experiment.

Depending on the incident energies, neutrons can have a higher cross-section than photons to produce fission in ^{238}U. The cross-section of neutron-induced fission reactions inside depleted uranium remains quite low in the mb range from epithermal to intermediate neutrons, with the exception of a few narrow absorption lines ranging up to 1 b. Nevertheless, the average cross-section in this region lies on the order of mb. On the other hand, the cross-section increases quickly for neutron energies above 1 MeV, where it reaches a plateau up to 1 GeV at around 1 b.[41] In this experiment, we expect the neutrons to be epithermal. Therefore, their energies do not reach the mentioned cross-section plateau. Nevertheless, a high number of thermal neutrons might effectively induce additional fission reactions.

In this experiment, neutrons originate from different reactions. Neutrons are produced by the fission process of uranium itself, by (γ, xn)-reactions inside the activatable targets, but also by (γ, xn)-reactions inside almost any material in the PHELIX laboratory that is exposed to high-energy photons. If we assume the expected reaction products from Sec. III A, we obtain an estimation of generated neutrons by the fission of uranium on the order of 10^4–10^5 particles. These neutrons are not sufficient to trigger a single additional fission reaction inside uranium. Therefore, these neutrons contribute less than 0.0001% to the total expected fission reactions, and is therefore, negligible. Based on the From the number of detected isotopes from the (γ, xn)-reactions inside the activatable targets, we can calculate the amount of neutrons that are produced by this process with 10^7 particles. If we assume an opening angle of these emerging neutrons similar to the photon opening angle, these neutrons could produce up to 10 fission reactions, which would contribute to our fission fragment decay spectrum with less than 0.1%. However, the neutrons most likely emerge in an isotropic manner. Therefore, this contribution is even lower than 0.1% and is negligible.

To determine the total number of neutrons, it is common in plasma physics to use bubble detectors.[44,45] In this experiment, we also took advantage of these detector types by using two bubble detectors. Their placement in the laboratory is shown in Fig. 1. The distance of these bubble detectors to the laser-matter interaction is 67 cm in the radial direction and 70.5 cm in the axial direction. With these bubble detectors, neutron numbers of 6.48×10^4 cm^{-2} in the axial direction and 3.77×10^4 cm^{-2} in the radial direction are detected. These numbers show a nearly isotropic distribution of the produced neutrons in this experiment. Under the assumption that these neutrons originate inside the PHELIX target chamber near the uranium targets, these numbers modify to an average total neutron abundance of 3.56×10^9 in the axial direction and 2.26×10^9 in the radial direction. With the radical assumption that these neutrons emerge at a distance of 1 cmto the first uranium target, roughly 10^8 neutrons could reach the uranium targets. This would lead to the generation of fission products on the order of 100 particles. These numbers would contribute less than 1% to our detected fission fragment decay spectrum, and are therefore, negligible. In addition to this calculated influence, the origin of the neutrons is expected to be distributed inside the whole PHELIX laboratory. Therefore, the actual portion of neutrons that reach our uranium targets is less than assumed. This leads to an even lower contribution of the $(\mathrm{n, fission})$-reactions to our detected fission fragment decay spectrum and therefore can be neglected. A neutron time-of-flight (ToF) diagnostic could provide further insights into the neutron spectrum and will be considered for future experiments.

IV. CONCLUSION AND SUMMARY

In this experiment, we produced fission isotopes using energetic laser-driven x-rays ($>$10 MeV) in depleted uranium targets. The x-rays were generated by bremsstrahlung from electrons accelerated via the DLA process in NCD foam targets. The x-ray intensity distribution and energy were measured using photon activation of a copper foil and backing squares of gold and tantalum targets. This information allowed us to calculate the total percentage of x-rays illuminating the uranium targets. In this experiment, the average percentage of x-rays illuminating the uranium targets was around 20% of the total X-ray cone intensity, indicating a well-directed x-ray beam. Per shot, we produced over 10^{11} photons. These x-rays induced fission reactions in the depleted uranium targets. The fission fragments were transported by a gas flow system to a liquid-nitrogen cooled activated carbon filter. Two HPGe detectors, positioned opposite each other, detected the decay of the captured fission fragments. In this experiment, we detected an average of approximately (345 ± 31) ^{139}Xe atoms per shot, which was the most prominent Xe isotope in this fission reaction. Additionally, flushing-out effects within the filter could play a significant role in this gas flow transport system. To verify flushing effects, the transportation times were used as an inverse flushing factor or more precisely a capturing factor. Using this factor, the correlation between the total expected fission yield, weighted by the capturing factor, and the actually detected ^{139}Xe isotopes was calculated with a Pearson's correlation coefficient of 0.81. This suggests the possibility of flushing effects within the cooled filter. Further cooling of the filter to increase capturing should be approached cautiously, as the boiling point of noble gases could be reached, clogging the filter. In addition to the correlation coefficient, the average cumulative yield probability of ^{139}Xe for this experiment was calculated to be (2.62 ± 120)% of the total expected fission yield. Comparing this value with the literature is complex, as the X-ray spectra of this experiment and the referenced comparison differ. Nonetheless, the cumulative yield probability trend decreases for more energetic X-ray spectra, aligning with our measured value.

ACKNOWLEDGMENTS

The results presented here are based on the experiment P-21-00005-ST, which was performed at the target station PTA at the GSI Helmholtzzentrum für Schwerionenforschung GmbH, Darmstadt (Germany) in the frame of FAIR Phase-0. This work has received funding by the European Union via the Euratom Research and Training Programme (Grant Agreement No 101052200—EUROfusion). The work of the authors affiliated with the Czech Technical University was supported by the Czech Science Foundation (Project No. GM23-05027M). Views and opinions expressed are, however, those of the author(s) only and do not necessarily reflect those of the European Union, the European Commission, or the Czech Science Foundation. Neither the European Union, the European Commission, nor the Czech Science Foundation can be held responsible for them. The authors would like to address special thanks to the group of the target laboratory at the GSI Helmholtzzentrum für Schwerionenforschung GmbH under the management of B. Lommel, for the production of the uranium targets. Also, special thanks go to the PHELIX Group, which contributed to the successful conduction of the experiment.

AUTHOR DECLARATIONS

Conflict of Interest

The authors have no conflicts to disclose.

Author Contributions

René Kalla: Formal analysis (lead); Project administration (equal); Software (equal); Supervision (equal); Visualization (lead); Writing – original draft (lead); Writing – review & editing (lead). **Wigen Nazarov:** Resources (lead). **Jan Novotny:** Formal analysis (supporting); Writing – review & editing (supporting). **Uwe Spillmann:** Writing – review & editing (supporting). **Dieter Schneider:** Conceptualization (equal); Writing – review & editing (supporting). **Alexander Yakushev:** Conceptualization (equal); Writing – review & editing (supporting). **Alex Zylstra:** Conceptualization (supporting); Writing – review & editing (supporting). **Olga N. Rosmej:** Conceptualization (equal); Supervision (supporting); Writing – review & editing (supporting). **Thomas U. Kuehl:** Conceptualization (equal); Writing – review & editing (supporting). **Vincent Bagnoud:** Conceptualization (lead); Writing – review & editing (supporting). **Pascal Boller:** Project administration (equal); Supervision (lead); Writing – review & editing (equal). **Parysatis M. Tavana:** Formal analysis (equal); Visualization (supporting); Writing – review & editing (equal). **Christian Brabetz:** Supervision (equal). **Jeffrey Burggraf:** Writing – review & editing (supporting). **Jakub Cikhardt:** Formal analysis (supporting); Writing – review & editing (supporting). **Jan Glorius:** Software (equal); Writing – review & editing (supporting). **Mikhail Gyrdymov:** Writing – review & editing (supporting). **Yuri A. Litvinov:** Writing – review & editing (supporting).

DATA AVAILABILITY

The DOI link for the available data will be created, once the paper is accepted.

REFERENCES

[1] F. Käppeler, F.-K. Thielemann, and M. Wiescher, "Current quests in nuclear astrophysics and experimental approaches," Annu. Rev. Nucl. Part. Sci. **48**, 175–251 (1998).

[2] T. Kawano, P. Talou, J. E. Lynn, M. B. Chadwick, and D. G. Madland, "Calculation of nuclear reaction cross sections on excited nuclei with the coupled-channels method," Phys. Rev. C **80**, 024611 (2009).

[3] A. Zilges, P. von Brentano, R.-D. Herzberg, U. Kneissl, J. Margraf, H. Maser, N. Pietralla, and H. H. Pitz, "Strong dipole excitations around 1.8 MeV in ^{238}U," Phys. Rev. C **52**, R468–R470 (1995).

[4] S. L. Hammond, A. S. Adekola, C. T. Angell, H. J. Karwowski, E. Kwan, G. Rusev, A. P. Tonchev, W. Tornow, C. R. Howell, and J. H. Kelley, "Dipole response of ^{238}U to polarized photons below the neutron separation energy," Phys. Rev. C **85**, 044302 (2012).

[5] O. N. Rosmej, M. Gyrdymov, M. M. Günther, N. E. Andreev, P. Tavana, P. Neumayer, S. Zähter, N. Zahn, V. S. Popov, N. G. Borisenko, A. Kantsyrev, A. Skobliakov, V. Panyushkin, A. Bogdanov, F. Consoli, X. F. Shen, and A. Pukhov, "High-current laser-driven beams of relativistic electrons for high-energy density research," Plasma Phys. Controlled Fusion **62**(11), 115024 (2020).

[6] M. M. Günther, O. N. Rosmej, P. Tavana, M. Gyrdymov, A. Skobliakov, A. Kantsyrev, S. Zähter, N. G. Borisenko, A. Pukhov, and N. E. Andreev, "Forward-looking insights in laser-generated ultra-intense γ-ray and neutron sources for nuclear application and science," Nat. Commun. **13**(1), 170 (2022).

[7] S. Carbajo, E. A. Nanni, L. J. Wong, G. Moriena, P. D. Keathley, G. Laurent, R. J. D. Miller, and F. X. Kärtner, "Direct longitudinal laser acceleration of electrons in free space," Phys. Rev. Accel. Beams **19**, 021303 (2016).

[8] P. Boller, A. Zylstra, P. Neumayer, L. Bernstein, C. Brabetz, J. Despotopulos, J. Glorius, J. Hellmund, E. A. Henry, J. Hornung, J. Jeet, J. Khuyagbaatar, L. Lens, S. Roeder, T. Stoehlker, A. Yakushev, Y. A. Litvinov, D. Shaughnessy, V. Bagnoud, T. Kuehl, and D. H. G. Schneider, "First on-line detection of radioactive fission isotopes produced by laser-accelerated protons," Sci. Rep. **10**(1), 17183 (2020).

[9] J. Wenz and S. Karsch, "Physics of laser-wakefield accelerators (LWFA)," arXiv:2007.04622, 2020.

[10] S. Chen, N. D. Powers, I. Ghebregziabher, C. M. Maharjan, C. Liu, G. Golovin, S. Banerjee, J. Zhang, N. Cunningham, A. Moorti, S. Clarke, S. Pozzi, and D. P. Umstadter, "MeV-energy x rays from inverse Compton scattering with laser-wakefield accelerated electrons," Phys. Rev. Lett. **110**, 155003 (2013).

[11] H.-Y. Lan, D. Wu, J.-X. Liu, J.-Y. Zhang, H.-G. Lu, J.-F. Lv, X.-Z. Wu, W. Luo, and X.-Q. Yan, "Photonuclear production of nuclear isomers using bremsstrahlung induced by laser-wakefield electrons," Nucl. Sci. Tech. **34**(5), 74 (2023).

[12] A. Pukhov, Z.-M. Sheng, and J. Meyer-ter-Vehn, "Particle acceleration in relativistic laser channels," Phys. Plasmas **6**(7), 2847–2854 (1999).

[13] A. Pukhov and J. Meyer-ter-Vehn, "Laser wake field acceleration: The highly non-linear broken-wave regime," Appl. Phys. B **74**(4), 355–361 (2002).

[14] O. N. Rosmej, X. F. Shen, A. Pukhov, L. Antonelli, F. Barbato, M. Gyrdymov, M. M. Günther, S. Zähter, V. S. Popov, N. G. Borisenko, and N. E. Andreev, "Bright betatron radiation from direct-laser-accelerated electrons at moderate relativistic laser intensity," Matter Radiat. Extremes **6**(4), 048401 (2021).

[15] J. Cikhardt, M. Gyrdymov, S. Zähter, P. Tavana, M. M. Günther, N. Bukharskii, N. Borisenko, J. Jacoby, X. F. Shen, A. Pukhov, N. E. Andreev, and O. N. Rosmej, "Characterization of bright betatron radiation generated by direct laser acceleration of electrons in plasma of near critical density," Matter Radiat. at Extremes **9**(2), 027201 (2024).

[16] A. Pukhov and J. Meyer-ter-Vehn, "Relativistic laser-plasma interaction by multi-dimensional particle-in-cell simulations," Phys. Plasmas **5**(5), 1880–1886 05 (1998).

[17] Z. Major, U. Eisenbarth, B. Zielbauer, C. Brabetz, J. B. Ohland, Y. Zobus, S. Roeder, D. Reemts, S. Kunzer, S. Götte, D. Neidherr, J. Hornung, P. Kewes, D. Schumacher, D. Beck, P. Hesselbach, M. Malki, P. Neumayer, K. Weyrich, A. Tauschwitz, and V. Bagnoud, "High-energy laser facility PHELIX at GSI: Latest advances and extended capabilities," High Power Laser Sci. Eng. **12**, e39 (2024).

[18] O. N. Rosmej, N. E. Andreev, S. Zähter, N. Zahn, P. Christ, B. Borm, T. Radon, A. Sokolov, L. P. Pugachev, D. Khaghani, F. Horst, N. G. Borisenko, G. Sklizkov, and V. G. Pimenov, "Interaction of relativistically intense laser pulses with long-scale near critical plasmas for optimization of laser based sources of MeV electrons and gamma-rays," New J. Phys. **21**(4), 043044 (2019).

[19] P. Tavana, N. Bukharskii, M. Gyrdymov, U. Spillmann, S. Zähter, J. Cikhardt, N. G. Borisenko, P. Korneev, J. Jacoby, C. Spielmann, N. E. Andreev, M. M. Günther, and O. N. Rosmej, "Ultra-high efficiency bremsstrahlung production

in the interaction of direct laser-accelerated electrons with high-Z material," Front. Phys. **11**, 1178967 (2023).

[20] H. R. Weller, M. W. Ahmed, and Y. K. Wu, "Nuclear physics research at the high intensity gamma-ray source (HI γS)," Nucl. Phys. News **25**(3), 19–24 (2015).

[21] L. Csige, D. M. Filipescu, T. Glodariu, J. Gulyás, M. M. Günther, D. Habs, H. J. Karwowski, A. Krasznahorkay, G. C. Rich, M. Sin, L. Stroe, O. Tesileanu, and P. G. Thirolf, "Exploring the multihumped fission barrier of ^{238}U via sub-barrier photofission," Phys. Rev. C **87**, 044321 (2013).

[22] J. Kleemann, N. Pietralla, U. Friman-Gayer, J. Isaak, O. Papst, K. Prifti, V. Werner, A. D. Ayangeakaa, T. Beck, G. Colò, M. L. Cortés, S. W. Finch, M. Fulghieri, D. Gribble, K. E. Ide, X. K.-H. James, R. V. F. Janssens, S. R. Johnson, P. Koseoglou, Krishichayan, D. Savran, and W. Tornow, "Gamma decay of the ^{154}Sm isovector giant dipole resonance: Smekal-Raman scattering as a novel probe of nuclear ground-state deformation," Phys. Rev. Lett **134**, 022503 (2025).

[23] K. A. Tanaka, K. M. Spohr, D. L. Balabanski, S. Balascuta, L. Capponi, M. O. Cernaianu, M. Cuciuc, A. Cucoanes, I. Dancus, A. Dhal, B. Diaconescu, D. Doria, P. Ghenuche, D. G. Ghita, S. Kisyov, V. Nastasa, J. F. Ong, F. Rotaru, D. Sangwan, P.-A. Söderström, D. Stutman, G. Suliman, O. Tesileanu, L. Tudor, N. Tsoneva, C. A. Ur, D. Ursescu, and N. V. Zamfir, "Current status and highlights of the ELI-NP research program," Matter Radiat. Extremes **5**(2), 024402 (2020).

[24] D. L. Balabanski and P. Constantin, "80 years of experimental photo-fission research," Eur. Phys. J. A **60**(2), 39 (2024).

[25] B. L. Berman and S. C. Fultz, "Measurements of the giant dipole resonance with monoenergetic photons," Rev. Mod. Phys. **47**, 713–761 (1975).

[26] W. D. Myers, W. J. Swiatecki, T. Kodama, L. J. El-Jaick, and E. R. Hilf, "Droplet model of the giant dipole resonance," Phys. Rev. C **15**, 2032–2043 (1977).

[27] V. Bagnoud, B. Aurand, A. Blazevic, S. Borneis, C. Bruske, B. Ecker, U. Eisenbarth, J. Fils, A. Frank, E. Gaul, S. Goette, C. Haefner, T. Hahn, K. Harres, H.-M. Heuck, D. Hochhaus, D. H. H. Hoffmann, D. Javorková, H.-J. Kluge, T. Kuehl, S. Kunzer, M. Kreutz, T. Merz-Mantwill, P. Neumayer, E. Onkels, D. Reemts, O. Rosmej, M. Roth, T. Stoehlker, A. Tauschwitz, B. Zielbauer, D. Zimmer, and K. Witte, "Commissioning and early experiments of the PHELIX facility," Appl. Phys. B **100**(1), 137–150 (2010).

[28] O. N. Rosmej, M. Gyrdymov, N. E. Andreev, P. Tavana, V. Popov, N. G. Borisenko, A. I. Gromov, S. Y. Gus'kov, R. Yakhin, G. A. Vegunova *et al.*, "Advanced plasma target from pre-ionized low-density foam for effective and robust direct laser acceleration of electrons," High Power Laser Sci. Eng. **13**, e3 (2025).

[29] X. F. Shen, A. Pukhov, M. M. Günther, and O. N. Rosmej, "Bright betatron X-rays generation from picosecond laser interactions with long-scale near critical density plasmas," Appl. Phys. Lett. **118**(13), 134102 (2021).

[30] S. Agostinelli, J. Allison, K. Amako, J. Apostolakis, H. Araujo, P. Arce, M. Asai, D. Axen, S. Banerjee, G. Barrand, F. Behner, L. Bellagamba, J. Boudreau, L. Broglia, A. Brunengo, H. Burkhardt, S. Chauvie, J. Chuma, R. Chytracek, G. Cooperman, G. Cosmo, P. Degtyarenko, A. Dell'Acqua, G. Depaola, D. Dietrich, R. Enami, A. Feliciello, C. Ferguson, H. Fesefeldt, G. Folger, F. Foppiano, A. Forti, S. Garelli, S. Giani, R. Giannitrapani, D. Gibin, J. J. Gómez Cadenas, I. González, G. Gracia Abril, G. Greeniaus, W. Greiner, V. Grichine, A. Grossheim, S. Guatelli, P. Gumplinger, R. Hamatsu, K. Hashimoto, H. Hasui, A. Heikkinen, A. Howard, V. Ivanchenko, A. Johnson, F. W. Jones, J. Kallenbach, N. Kanaya, M. Kawabata, Y. Kawabata, M. Kawaguti, S. Kelner, P. Kent, A. Kimura, T. Kodama, R. Kokoulin, M. Kossov, H. Kurashige, E. Lamanna, T. Lampén, V. Lara, V. Lefebure, F. Lei, M. Liendl, W. Lockman, F. Longo, S. Magni, M. Maire, E. Medernach, K. Minamimoto, P. Mora de Freitas, Y. Morita, K. Murakami, M. Nagamatu, R. Nartallo, P. Nieminen, T. Nishimura, K. Ohtsubo, M. Okamura, S. O'Neale, Y. Oohata, K. Paech, J. Perl, A. Pfeiffer, M. G. Pia, F. Ranjard, A. Rybin, S. Sadilov, E. Di Salvo, G. Santin, T. Sasaki, N. Savvas, Y. Sawada, S. Scherer, S. Sei, V. Sirotenko, D. Smith, N. Starkov, H. Stoecker, J. Sulkimo, M. Takahata, S. Tanaka, E. Tcherniaev, E. Safai Tehrani, M. Tropeano, P. Truscott, H. Uno, L. Urban, P. Urban, M. Verderi, A. Walkden, W. Wander, H. Weber, J. P. Wellisch, T. Wenaus, D. C. Williams, D. Wright, T. Yamada, H. Yoshida, and D. Zschiesche, "Geant4—a simulation toolkit," Nucl. Instrum. Methods Phys. Res., Sec. A **506**(3), 250–303 (2003).

[31] J. A. Anderson, C. D. Eberhard, K. N. Taylor, J. M. Carroll, J. J. Carroll, M. J. Byrd, and C. B. Collins, "Spectral characterization of intense, short duration bremsstrahlung pulses with nuclear photoactivation techniques," IEEE Trans. Nucl. Sci. **36**(1), 241–245 (1989).

[32] M. M. Günther, K. Sonnabend, E. Brambrink, K. Vogt, V. Bagnoud, K. Harres, and M. Roth, "A novel nuclear pyrometry for the characterization of high-energy bremsstrahlung and electrons produced in relativistic laser-plasma interactions," Phys. Plasmas **18**(8), 083102 (2011).

[33] I. Spencer, K. W. D. Ledingham, R. P. Singhal, T. McCanny, P. McKenna, E. L. Clark, K. Krushelnick, M. Zepf, F. N. Beg, M. Tatarakis, A. E. Dangor, R. D. Edwards, M. A. Sinclair, P. A. Norreys, R. J. Clarke, and R. M. Allott, "A nearly real-time high temperature laser–plasma diagnostic using photonuclear reactions in tantalum," Rev. Sci. Instrum. **73**(11), 3801–3805 (2002).

[34] J. F. Ziegler, "SRIM-2003," in Proceedings of the Sixteenth International Conference on Ion Beam Analysis, 2004 , [Nucl. Instrum. Methods Phys. Res., Sect. B **219–220**, 1027–1036 (2004)].

[35] J. F. Ziegler, M. D. Ziegler, and J. P. Biersack, "SRIM—The stopping and range of ions in matter (2010)," Nucl. Instrum. Methods Phys. Res., Sect. B **268**(11), 1818–1823 (2010). 19th International Conference on Ion Beam Analysis.

[36] K. Masumoto and C. Segebade, *Photon Activation Analysis* (John Wiley & Sons, Ltd., 2006).

[37] C. Segebade, H. P. Weise, G. J. Lutz, and F. Adams, "Photon activation analysis," Anal. Chim. Acta **211**, 339–339 (1988).

[38] C. Segebade, H. P. Weise, and G. J. Lutz. *Photon Activation Analysis* (De Gruyter, 2011). URL https://books.google.com.au/books?id=Nja4D-ooBAUC.

[39] J.-H. Chao, P.-C. Hsu, and H.-M. Liu, "Measurement of high dose rates by photon activation of indium foils," Appl. Radiat. Isot. **55**(4), 549–556 (2001).

[40] A. Koning, S. Hilaire, and S. Goriely, "TALYS: Modeling of nuclear reactions," Eur. Phys. J. A **59**(6), 131 (2023).

[41] O. Iwamoto, N. Iwamoto, S. Kunieda, S. Nakayama, F. Minato, Y. Abe, K. Tsubakihara, S. Okumura, C. Ishizuka, T. Yoshida, S. Chiba, N. Otuka, J.-C. Sublet, H. Iwamoto, K. Yamamoto, Y. Nagaya, K. Tada, C. Konno, N. Matsuda, K. Yokoyama, H. Taninaka, A. Oizumi, M. Fukushima, S. Okita, G. Chiba, S. Sato, M. Ohta, and S. Kwon, "Japanese evaluated nuclear data library version 5: JENDL-5," J. Nucl. Sci. Technol. **60**(1), 1–60 (2023).

[42] O. Iwamoto, N. Iwamoto, S. Kunieda, F. Minato, and K. Shibata, "The CCONE code system and its application to nuclear data evaluation for fission and other reactions," Nucl. Data Sheets **131**, 259–288 (2016).

[43] A. Foley and H. Yang, "Short-lived photofission product yields from 238U and 232Th at bremsstrahlung X-ray endpoint energies of 8, 14, and 20 MeV for nuclear forensics isotope production applications," Nucl. Instrum. Methods Phys. Res., Sec. A **1013**, 165621 (2021).

[44] D. Jung, K. Falk, N. Guler, O. Deppert, M. Devlin, A. Favalli, J. C. Fernandez, D. C. Gautier, M. Geissel, R. Haight, C. E. Hamilton, B. M. Hegelich, R. P. Johnson, F. Merrill, G. Schaumann, K. Schoenberg, M. Schollmeier, T. Shimada, T. Taddeucci, J. L. Tybo, S. A. Wender, C. H. Wilde, G. A. Wurden, and M. Roth, "Characterization of a novel, short pulse laser-driven neutron source," Phys. Plasmas **20**(5), 056706 (2013).

[45] A. Kleinschmidt, V. Bagnoud, O. Deppert, A. Favalli, S. Frydrych, J. Hornung, D. Jahn, G. Schaumann, A. Tebartz, F. Wagner, G. Wurden, B. Zielbauer, and M. Roth, "Intense, directed neutron beams from a laser-driven neutron source at PHELIX," Phys. Plasmas **25**(5), 053101 (2018).